Chemical Science

ROYAL SOCIETY OF CHEMISTRY

EDGE ARTICLE

View Article Online
View Journal

Cite this: DOI: 10.1039/d6sc02936a

All publication charges for this article have been paid for by the Royal Society of Chemistry

d-Orbital modulation of high-entropy sulfides with amorphous/crystalline heterostructures for simultaneous hydrogen production and sulfur recovery

Ruotong Liu,[a] Jingying Li,[a] Yu Pang,[a] Yanru Liu,[a] Xiaolong Wang,[a] Dan Zhang,*[b] Hongdong Li*[a] and Lei Wang*[a]

Replacing the anodic oxygen evolution reaction (OER) with the sulfur oxidation reaction (SOR) presents a promising strategy for energy-saving hydrogen production and simultaneous treatment of sulfur-rich wastewater. However, the adsorption and accumulation of sulfur intermediates on catalyst surfaces often lead to active-site poisoning and structural corrosion, severely hindering practical implementation. Herein, we report a novel amorphous/crystalline high-entropy sulfide (FeCoNiMnMg–S) heterostructure synthesized *via* a facile room-temperature corrosion method. This amorphous/crystalline structure not only enhances charge transfer at the heterointerface but also triggers electronic rearrangement of the M-site d-orbitals. This facilitates electron transitions from the t_{2g} orbitals to the e_g orbitals, achieving a half-filled electronic configuration that optimizes the adsorption of sulfur intermediates at the M-site. Benefiting from this electronic structure modulation, the catalyst exhibits exceptional bifunctional activity for both the hydrogen evolution reaction (HER) and SOR, achieving an ultra-low cell voltage of only 1.04 V to deliver 1000 mA cm^{-2}, along with outstanding operational stability over 200 hours at high current density. This work provides a new paradigm for designing highly efficient and robust electrocatalysts that enable sustainable hydrogen production and synchronous sulfur recycling in a single system.

Received 9th April 2026
Accepted 24th May 2026

DOI: 10.1039/d6sc02936a

rsc.li/chemical-science

Introduction

Hydrogen energy has emerged as a pivotal clean energy carrier due to its high energy density and zero carbon emission.[1–3] Electrochemical water splitting represents a sustainable pathway for hydrogen production, yet its efficiency is severely hampered by the anodic oxygen evolution reaction (OER), a kinetically sluggish four-electron process that demands high overpotential and considerably elevates energy consumption.[4–8] To circumvent this limitation, replacing the OER with thermodynamically favorable small-molecule oxidation reactions such as the urea oxidation reaction (UOR), methanol oxidation reaction (MOR), or sulfur oxidation reaction (SOR) has attracted growing interest (Fig. S1).[9–12] Among these, the SOR ($S^{2-} \rightarrow S + 2e^-$, −0.48 V *vs.* the Reversible Hydrogen Electrode (RHE)) is particularly appealing, as it not only reduces the energy input for hydrogen generation but also enables concurrent detoxification and valorization of sulfur-containing wastewater, achieving a "one-stone-two-birds" outcome.

Nevertheless, the practical deployment of the SOR faces critical challenges rooted in catalyst deactivation. Sulfur species and intermediates tend to adsorb and accumulate on catalyst surfaces, leading to rapid active-site poisoning, severe corrosion, and irreversible deactivation.[13,14] These issues result in dramatic activity decay and poor operational stability, especially at the high sulfur concentrations necessary for practical applications. Therefore, the development of robust electrocatalysts that combine high intrinsic activity for the SOR with exceptional resistance to sulfur poisoning and corrosion is urgently required but remains a significant hurdle.

High-entropy materials (HEMs), incorporating multiple principal elements in near-equimolar ratios, offer unique advantages for electrocatalysis, including enhanced structural stability, tunable electronic properties, and entropic stabilization effects.[15–19] In particular, high-entropy sulfides (HESs) combine these merits with high electrical conductivity and inherent compatibility with sulfur electrolytes.[20–24] Meanwhile, constructing amorphous/crystalline (a–c) hetero-interfaces has been demonstrated to combine the advantages of both phases,

[a]*Key Laboratory of Eco-Chemical Engineering, International Science and Technology Cooperation Base of Eco-Chemical Engineering and Green Manufacturing, College of Chemistry and Molecular Engineering, Qingdao University of Science and Technology, Qingdao, P. R. China. E-mail: hdli@qust.edu.cn; inorchemwl@126.com*

[b]*Key Laboratory of Catalytic Conversion and Clean Energy in Universities of Shandong Province, School of Chemistry and Chemical Engineering, Qufu Normal University, Qufu, P. R. China. E-mail: zhangdan@qfnu.edu.cn*

not only ensuring excellent conductivity and structural stability but also generating abundant active sites, which optimize intermediate adsorption and accelerate reaction kinetics.[25–28] Additionally, the sulfur oxidation intermediates existing in molecular form have a strong interaction with the d orbitals of the catalyst. Typically, the t_{2g} orbitals (d_{xz}, d_{yz}, and d_{zy}) and the e_g orbitals (d_{z^2} and $d_{x^2-y^2}$) play a key role in controlling intermediate binding.[29–31] Nevertheless, how the complex chemical environment in high-entropy systems, especially at the a–c interface, orchestrates orbital-level electron rearrangement to simultaneously enhance catalytic activity and alleviate sulfur poisoning remains poorly understood. This poses a significant challenge for the rational design of durable and highly active SOR-assisted hydrogen production catalysts.

In this work, we overcome the aforementioned challenges through the rational design and synthesis of a self-supported amorphous/crystalline high-entropy sulfide (FeCoNiMnMg–S) electrode *via* a scalable room-temperature corrosion strategy. This unique high-entropy heterogeneous structure not only exposes a high density of active sites but also facilitates efficient electron transport and exhibits outstanding corrosion resistance. Density functional theory (DFT) calculations demonstrate that interfacial charge transfer drives electron migration from the t_{2g} to the e_g orbitals, creating a favorable half-filled electronic configuration. This orbital engineering effectively optimizes the adsorption strength of sulfur intermediates, thereby accelerating SOR kinetics while alleviating catalyst poisoning. The synergistic combination of high-entropy stabilization and the a–c heterostructure endows the catalyst with exceptional activity and durability. As a result, the obtained catalyst demonstrates superior HER and SOR activity, requiring an ultra-low cell voltage of 1.04 V to achieve 1000 mA cm^{-2}, along with remarkable durability over 200 hours of continuous operation. This work offers a feasible and efficient materials design strategy towards high-performance electrocatalysts for sustainable hydrogen production and environmental remediation.

Results and discussion

Fig. 1 shows the process of *in situ* growth of FeCoNiMnMg–S nanosheet arrays on nickel foam (NF) substrates *via* corrosion engineering. Specifically, metal salts and sodium thiosulphate are first added to deionized water to form a clear solution. Then, NF is placed in the uniformly dispersed solution and etched at room temperature for 2 hours. After etching, NF visibly turns brownish-green, indicating the successful synthesis of high-entropy sulfides on NF (Fig. S2). Since the room-temperature corrosion synthesis route is easily scalable, we conducted corresponding scale-up experiments. Fig. S3a shows a digital photograph of the scaled-up NF (10 × 10 cm^2) after the corrosion process. By observing the scaled-up NF at four arbitrary locations using a scanning electron microscope (SEM), we found that the morphology of the prepared material was relatively uniform (Fig. S3b–e). Unlike the smooth bare NF surface (Fig. S4), the synthesized high-entropy sulfide nanosheets grow vertically and densely on the NF surface, with a thickness of approximately 5.84 nm and have a large number of cavities (Fig. 2a–c and S5), which is conducive to mass transfer and gas release.[32] This nanoscale layered structure effectively promotes interaction between the catalyst and the support and exhibits good electrical conductivity.[33] To investigate the role of metal elements in the synthesis of nanosheets, we additionally synthesized ternary and quaternary catalysts (FeCoNi–S and FeCoNiMg–S). The results obtained by SEM showed that the presence of Mg elements was beneficial for the growth of cavity-rich nanosheets (Fig. S6).

The crystalline phases of the prepared samples were characterized by X-ray diffraction (XRD). Fig. 2d and S7 show the XRD patterns of FeCoNiMnMg–S and the corresponding ternary and quaternary metal sulfides. The main diffraction peaks of all metal sulfide catalysts are broadly consistent with those of NiS_2 (PDF #11-0099). However, compared with pure NiS_2, the diffraction peaks of FeCoNiMnMg–S exhibit a systematic, slight shift towards lower angles, with a slight increase in half-width. This phenomenon is entirely consistent with the lattice expansion and microstrain caused by multi-element doping. As observed from the transmission electron microscopy (TEM) image (Fig. 2e), the surface of FeCoNiMnMg–S nanosheets exhibits numerous wrinkles, which is consistent with the SEM images. The wrinkled nanosheets can further provide more electrochemical active sites, thereby enhancing catalytic activity.[34] The crystal structure of FeCoNiMnMg–S was analyzed in detail using high-resolution transmission electron microscopy (HRTEM). As shown in Fig. 2f, FeCoNiMnMg–S exhibits a disordered structure with both crystalline and amorphous regions. Upon magnification, it can be observed that the crystalline region exhibits distorted lattice striations with a spacing of 0.2840 nm due to elemental doping. This is also consistent with the weaker intensity and broader diffraction peaks observed in the XRD results. Further ICP and TEM mapping analysis was conducted to investigate the distribution of each element and content in FeCoNiMnMg–S (Fig. 2g and Table S1). The results show that the element distribution is uniform and consistent with the SEM mapping (Fig. S8 and S9). Furthermore, through SEM observation, it was found that the ternary FeCoNi–S catalyst began to exhibit wrinkled morphology, while the quaternary FeCoNiMg–S catalyst began to show nanosheets (Fig. S10 and S11). When other high-entropy combinations (FeCoNiMnAl–S, FeCoNiMnCu–S, and FeCoNiMnCr–S) were used, no nanosheet morphology appeared (Fig. S12). This indicates that the Mg element plays an important role in the formation of the nanosheet morphology.

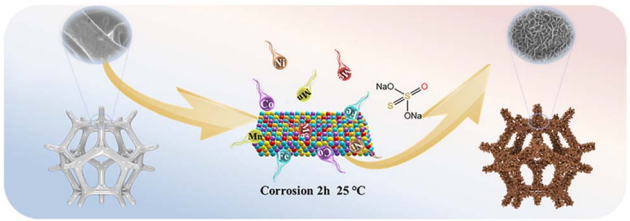

Fig. 1 Schematic diagram for the synthesis of FeCoNiMnMg–S.

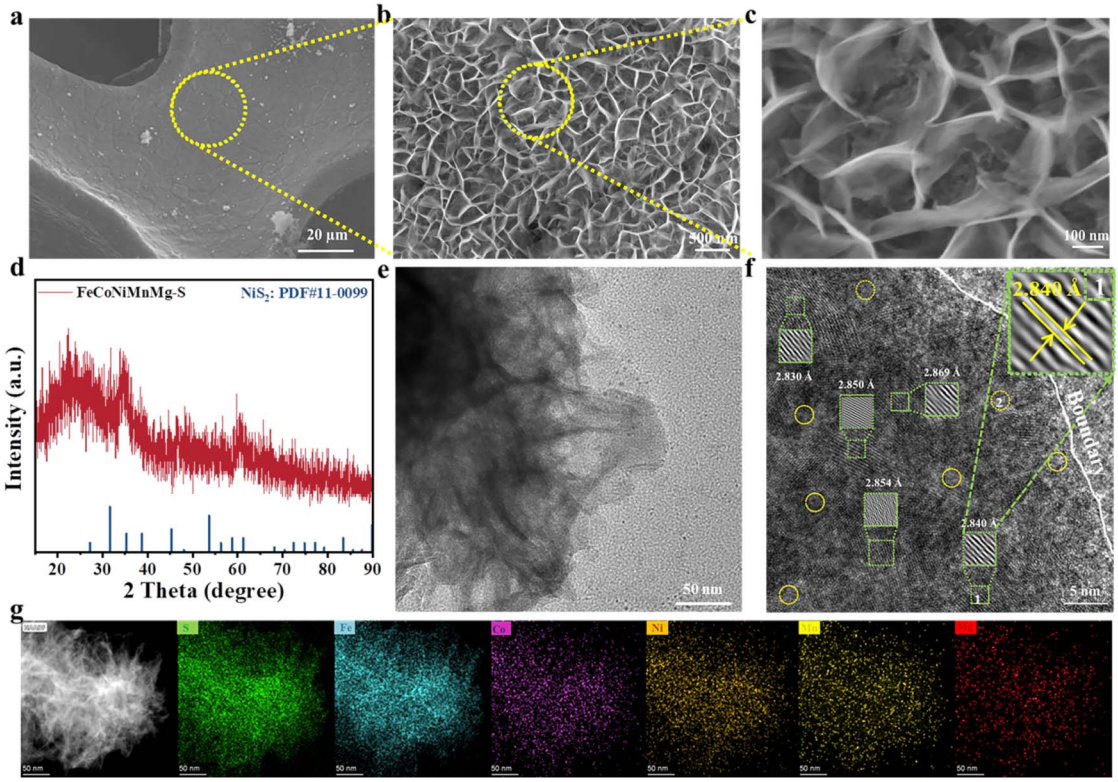

Fig. 2 (a–c) SEM images, (d) XRD pattern, and (e) TEM and (f) HRTEM images of FeCoNiMnMg–S (the yellow wire frame is the amorphous area; inset: the selected crystalline area in (g) is magnified), and (g) HADDF-STEM image of FeCoNiMnMg–S and corresponding EDS elemental mapping (Fe, Co, Ni, Mn, Mg, and S).

The composition and valence states of the prepared catalysts (FeCoNiMnMg–S, FeCoNiMg–S, and FeCoNi–S) were analyzed using X-ray photoelectron spectroscopy (XPS) (Fig. S13–S15). The XPS spectrum of FeCoNiMnMg–S is shown in Fig. S15, where the Fe 2p spectrum is divided into Fe $2p_{1/2}$ and Fe $2p_{3/2}$; the peaks near 711.0 eV (Fe $2p_{3/2}$) and 724.0 eV (Fe $2p_{1/2}$) correspond to Fe^{2+}, while the peaks at 713.5 eV (Fe $2p_{3/2}$) and 726.6 eV (Fe $2p_{1/2}$) are attributed to the presence of Fe^{3+}.[35–37] Fig. S15b shows the XPS spectrum of Co 2p, where the Co $2p_{3/2}$ (Co^{2+}/Co^{3+}) peak is deconvoluted into two peaks at 782.8 and 780.8 eV, the Co $2p_{1/2}$ (Co^{2+}/Co^{3+}) peak is located at 798.3 and 796.3 eV, and the two peaks at 786.6 and 803.4 eV are satellite peaks.[38–40] Similarly, Fig. S15c shows the XPS spectrum of Ni 2p, where the peaks at 855.5 eV (Ni $2p_{3/2}$) and 873.3 eV (Ni $2p_{1/2}$) confirm the presence of Ni^{2+}, while the peaks near 856.7 eV (Ni $2p_{3/2}$) and 874.5 eV (Ni $2p_{1/2}$) indicate the presence of Ni^{3+}. Additionally, the two small peaks at 870.0 eV and 852.5 eV belong to Ni^0, while the peaks near 861.6 and 880.3 eV correspond to the two satellite peaks of Ni.[41–43] The Mn $2p_{3/2}$ peak can be deconvoluted into three peaks, standing for Mn^{2+} (639.4 eV), Mn^{3+} (642.2 eV) and Mn^{4+} (645.1 eV), respectively, which reveals that the Mn ions in FeCoNiMnMg–S are predominantly in the oxidation states of +3.[44–46] In the Mg 1s spectrum, only a broad peak at 1304.1 eV is present.[47,48]

Compared to FeCoNi–S, the addition of Mn and Mg elements causes Fe, Co, and Ni to shift toward lower binding energies. This is because the electronegativity differences between Mn (1.55), Mg (1.31), and Fe (1.83), Co (1.88), and Ni (1.91) are significant. Electrons transfer from the lower electronegativity Mn and Mg to the higher electronegativity Ni, Fe, and Co, resulting in strong local electron interactions. Under these conditions, the electron density around the electron acceptor increases, reducing the adsorption energy of the product and reaction intermediates, thereby enhancing the catalytic activity of high-entropy sulfides.[49,50] In addition, in the S 2p spectrum (Fig. S15f), the peak appears at binding energies of 162.0, 162.9, and 163.7 eV, corresponding to S^{2-} $2p_{3/2}$, S^{2-} $2p_{1/2}$, and S_2^{2-} substances respectively, whereas the peak at 168.7 eV is designated as an S–O bond originating from atmospheric oxidation of the S_2 surface to SO_4^{2-} species.[51–53] We further distinguished whether the amorphous regions were 'intrinsic amorphous sulphide phases' or 'surface oxide layers' by means of Ar^+ etching XPS depth profiling. After the Ar^+ etching, the oxide layer was gradually stripped away, exposing the underlying unoxidised crystalline sulphide. As can be seen in Fig. S16, the signals for S–O species (such as SO_4^{2-}) rapidly decayed; this indicates that S–O species are present only in the very shallow surface layer, further ruling out the possibility that the amorphous regions are equivalent to the surface oxide layer.

To determine the performance advantages of high-entropy FeCoNiMnMg–S, the performance was first tested in NaOH solution. FeCoNiMnMg–S exhibited outstanding OER catalytic activity in 1.0 M NaOH, achieving an overpotential of only 275 mV at 100 mA cm^{-2} with a Tafel slope of 30.97 mV dec^{-1},

significantly outperforming FeCoNiMg–S, FeCoNi–S, RuO_2, and NF (Fig. 3a, b and S17). To explore the origin of this high activity, we investigated its double-layer capacitance and charge transfer characteristics. The double-layer capacitance (C_{dl}) was derived from Cyclic Voltammetry (CV) curves (Fig. S18), and the electrochemical surface area (ECSA) was subsequently estimated (Fig. S19a). The C_{dl} of FeCoNiMnMg–S (4.07 mF cm^{-2}) was markedly higher than that of all comparison samples, indicating that the enhanced OER performance is primarily attributable to an increased number of active sites. To assess whether the activity enhancement depends solely on this increase, we further analyzed ECSA-normalized polarization curves (Fig. S19b and c). FeCoNiMnMg–S still displayed a lower overpotential after normalization, confirming that the introduction of Mn and Mg not only generates new active sites but also enhances their intrinsic activity.[54–57] To further validate this intrinsic activity, we quantified the active sites electrochemically and estimated the turnover frequency (TOF), revealing the intrinsic catalytic performance on a per-site basis.[58,59] Since the TOF value is calculated based on the estimated number of active sites derived from the electrochemical double-layer capacitance and given the inherent assumptions in ECSA measurements (such as the uniform distribution of surface active sites), this value should be regarded as a semi-quantitative indicator. It is primarily used for relative comparisons of the intrinsic activity of catalysts, rather than as a precise measure of absolute activity. As shown in Fig. S20, when the overpotential was 350 mV, the TOF of FeCoNiMnMg–S was 0.224 s^{-1}, higher than that of the other catalysts, indicating that FeCoNiMnMg–S possesses higher intrinsic OER activity. Additionally, the charge transport behavior of FeCoNiMnMg–S was investigated using electrochemical impedance spectroscopy (EIS). As shown in Fig. S21, the interfacial charge transfer resistance (R_{ct}) of FeCoNiMnMg–S is reduced compared to low-entropy/medium-entropy catalysts, indicating an enhanced charge transfer rate.

Stability is also one of the most important criteria for OER performance. Long-term durability was evaluated by chronoamperometry at 100 mA cm^{-2}; after 100 h of continuous electrolysis. FeCoNiMnMg–S exhibited only 7.16% current attenuation (Fig. S22), and its Linear Sweep Voltammetry (LSV)

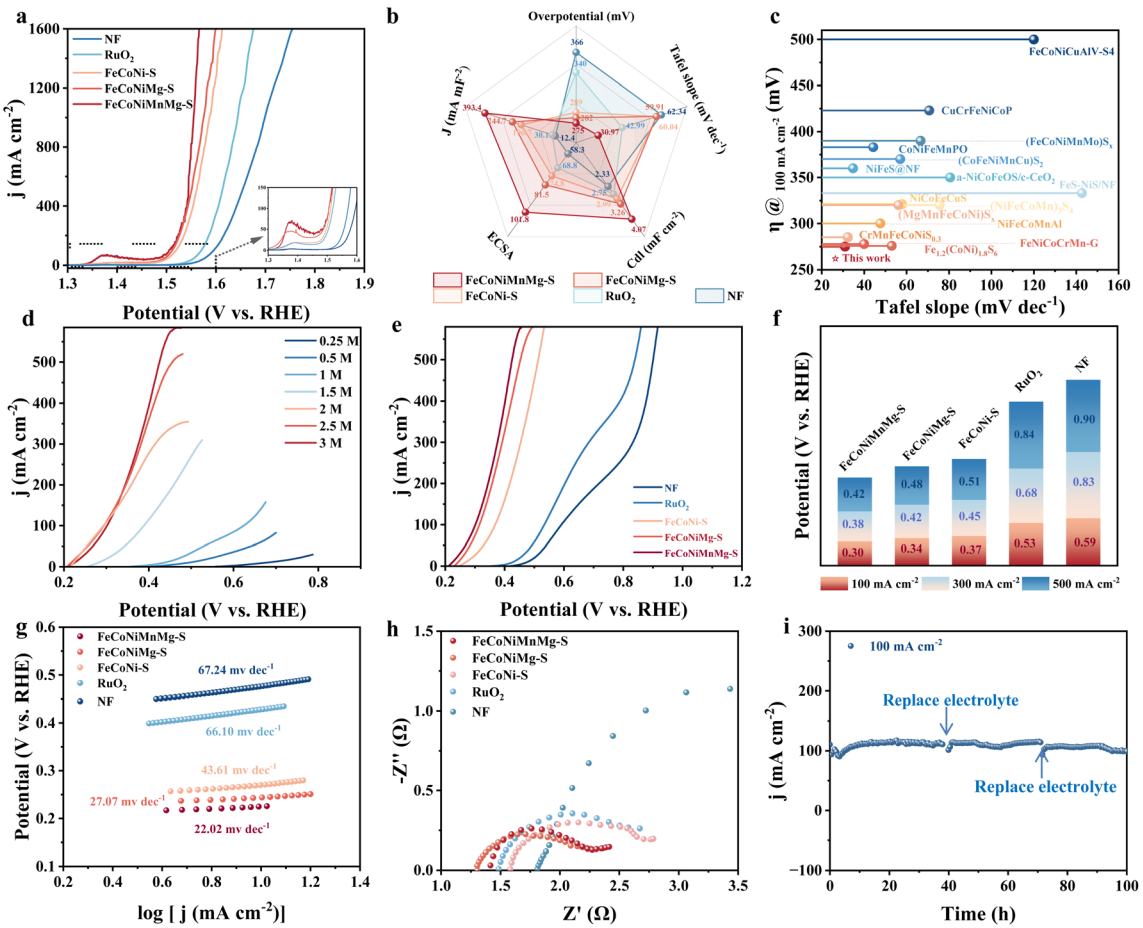

Fig. 3 (a) LSV curves of the prepared catalyst, (b) comparison of OER performance among different catalysts, (c) comparison of overpotential and Tafel slope at 100 mA cm^{-2} with those of previously reported electrocatalysts, (d) SOR polarization curves of FeCoNiMnMg–S in 1.0 M NaOH solutions containing different Na_2S concentrations (0–3.0 M), (e) current density of FeCoNiMnMg–S, FeCoNiMg–S, FeFCoNi–S, RuO_2 and NF in the SOR, (f) the potential comparison of the prepared catalysts in the SOR at current densities of 100, 300 and 500 mA cm^{-2}, (g) Tafel curves calculated from SOR polarization curves, (h) Nyquist plots of FeCoNiMnMg–S, FeCoNiMg–S, FeCoNi–OH, RuO_2 and NF, and (i) stability test of FeCoNiMnMg–S in 1.0 M NaOH + 3.0 M Na_2S for 100 h.

curve remained virtually unchanged from that of the pre-test state (Fig. S23), confirming excellent operational stability. In summary, FeCoNiMnMg–S possesses advantages such as low overpotential, small Tafel slope, numerous active sites, and fast charge transfer rate, exhibiting the best OER catalytic performance among the prepared HES samples. Furthermore, the OER activity of the FeCoNiMnMg–S catalyst surpasses that of most precious metal catalysts and non-precious metal catalysts (Fig. 3c and Table S2).

Although the OER performance of the catalyst is relatively good, the complex four-electron transfer process involved in the OER still requires a large overpotential to drive it. Therefore, we replaced the OER with the SOR and investigated the electrocatalytic performance of the prepared catalyst for anodic SOR in a 1.0 M NaOH solution containing Na_2S in the same three-electrode system mentioned above. As shown in Fig. 3d, the SOR performance of FeCoNiMnMg–S was tested in solutions of varying concentrations of Na_2S. The results revealed that as the concentration of sodium sulfide increased, the performance improved. When the concentration reached 3.0 M Na_2S, the SOR efficiency of the FeCoNiMnMg–S sample was nearly identical to that of the 2.5 M Na_2S sample. However, the SOR efficiency increased significantly at high current densities. Upon further increasing the concentration to 3.5 M, the test results indicated that the catalyst's SOR performance at 3.5 M was slightly lower than that at 3.0 M. Furthermore, during the testing process, white crystals were observed to precipitate in the electrochemical cell, which can be attributed to S^{2-} ($S^{2-} + H_2O \leftrightarrow HS^- + OH^-$; $HS^- + H_2O \leftrightarrow H_2S + OH^-$) (Fig. S24).[21,35] These precipitated crystals coated the electrode surface, significantly affecting the catalytic reaction process and leading to a decline in SOR performance. Therefore, we set the test concentration at 1.0 M NaOH + 3.0 M Na_2S. To compare with the other catalysts, we tested the catalytic activity of the control catalysts (FeCoNiMg–S, FeCoNi–S, RuO_2, and NF) in an electrolyte solution of 1.0 M NaOH + 3.0 M Na_2S. As shown in Fig. 3e and f, compared to the other catalysts, FeCoNiMnMg–S exhibited higher SOR catalytic activity, achieving current densities of 100 and 500 mA cm^{-2} at low potentials of 0.30 and 0.42 V *vs.* RHE, respectively. In addition, the current density struggles to increase further at higher potentials due to mass transfer limitations of the reactants (S^{2-}/HS^-), diffusion hindrance caused by polysulphide accumulation, the sulphide passivation layer on the electrode surface, and the coverage of active sites by elemental sulphur; consequently, a plateau region appears in the polarisation curve.[21,60,61] The Tafel slope was plotted and analyzed based on the LSV curve to investigate the catalytic kinetics of the SOR. As shown in Fig. 3g, the Tafel slope of FeCoNiMnMg–S is 22.02 mV dec^{-1}, which is lower than that of FeCoNiMg–S (27.07 mV dec^{-1}), FeCoNi–S (43.61 mV dec^{-1}), RuO_2 (66.1 mV dec^{-1}), and NF (67.24 mV dec^{-1}), indicating its excellent SOR kinetic performance. In addition, EIS revealed that FeCoNiMnMg–S had the lowest R_{ct} and the fastest charge transfer rate (Fig. 3h). To gain a deeper understanding of the intrinsic activity of the sample, the TOF was calculated by integrating the cyclic charge capacity obtained from the cyclic voltammetry curves to quantify the number of active sites. In Fig. S25, the calculated TOF is plotted against the potential for the SOR.

FeCoNiMnMg–S exhibits the highest TOF values at the same SOR potentials, indicating that this catalyst possesses higher catalytic activity than FeCoNiMg–S and FeCoNi–S. More importantly, the high-entropy sulfide nanosheet structure exhibits excellent SOR durability, as demonstrated by the chronoamperometric method. During continuous electrolysis at a current density of 100 mA cm^{-2} for 100 hours, the overpotential undergoes only minor changes (Fig. 3i). Moreover, the performance of the FeCoNiMnMg–S catalyst is not only superior to that of the recently reported catalysts (Fig. S26 and Table S3), but also the best when compared with other catalysts prepared from high-entropy compositions (Fig. S27). SEM, XRD, and XPS spectra confirm that the phase structure, morphology, and composition of the high-entropy sulfide catalyst remain virtually unchanged after SOR testing (Fig. S28–S30). This further validates the catalytic stability of the high-entropy sulfide nanosheet structure during the SOR process. The penetration of the electrolyte into the FeCoNiMnMg–S electrode was also assessed using contact angle measurements. The bare NF exhibited hydrophobic properties, with a contact angle of 128°. In contrast, the FeCoNiMnMg–S electrode exhibits superhydrophilic behavior, with a contact angle approaching 0° (Fig. S31). Therefore, it can closely come into contact with the electrolyte, which is beneficial for mass transfer.[62] These results demonstrate that FeCoNiMnMg–S electrodes exhibit outstanding SOR activity and stability, possessing the potential to reduce hydrogen production energy consumption by replacing the anodic OER.

To gain deeper insight into the influence of the FeCoNiMnMg–S a–c interface on the electronic structure and the underlying mechanism for its superior SOR performance, density functional theory (DFT) calculations were performed. Fig. 4a shows the theoretical calculation model of FeCoNiMnMg–S. To explain the mechanism of enhanced interfacial activity between crystalline and amorphous phases, the differential charge density distribution was studied, with depletion and accumulation regions shown in blue and yellow, respectively (Fig. 4b). It was found that there was a large amount of charge accumulation and depletion at the FeCoNiMnMg–S heterojunction, while NiS_2 exhibited relatively lower charge accumulation and depletion. The substantial electron accumulation at the heterojunction may lead to the formation of a built-in electric field, which could significantly enhance charge transfer and accelerate the reaction kinetics. To further understand the synergistic effects of multiple sites on the electronic structure of FeCoNiMnMg–S catalysts, the density of states (DOS) for each element was calculated (Fig. 4c). The results reveal a significant increase in the electron density of the metal orbitals near the Fermi level. In the SOR, a higher electron density near the Fermi level facilitates electron transfer and can strengthen the adsorption of reaction intermediates at the active site.[63,64] While pure NiS_2 exhibits symmetric spin-up and spin-down electron densities (Fig. S32), FeCoNiMnMg–S displays clear asymmetry, indicating the presence of numerous unpaired electrons. As shown in Fig. 4d, e and S33, the d-

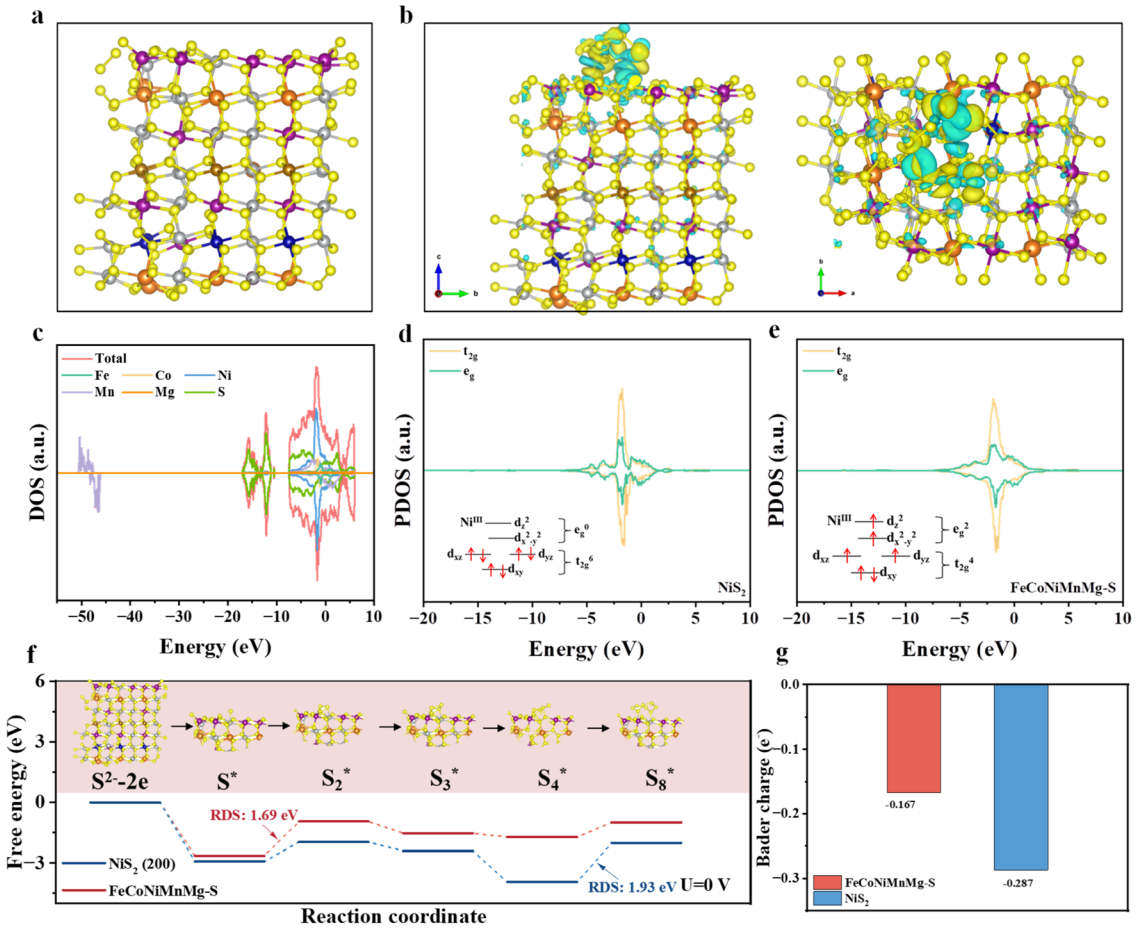

Fig. 4 (a) Theoretical model of FeCoNiMnMg–S and (b) the corresponding differential charge density distribution map at the interface. Cyan: Co, orange: Mg, brown: Fe, purple: Mn, silver: Ni, and yellow: S, (c) the density of states of FeCoNiMnMg–S, (d and e) PDOS and schematic diagrams of electron arrangement of t_{2g} and e_g orbitals of Ni in NiS_2 and FeCoNiMnMg–S, (f) free energy for the SOR pathways on NiS_2 and FeCoNiMnMg–S at $U = 0$ V, and (g) Bader charge analysis on FeCoNiMnMg–S and NiS_2.

electron occupation and the degenerate states of molecular orbitals reveal that the peak area of the e_g orbitals in FeCoNiMnMg–S is significantly larger than that in NiS_2. This is attributed to the a–c interface triggering the rearrangement of 3d orbital electrons at the M site, promoting the electron transition from the t_{2g} orbitals to the e_g orbitals to achieve a semi-filled state. Such rearrangement may optimize the adsorption of sulfur intermediates at the M site.[31] In summary, the Ni 3d orbital electron rearrangement induced by the a–c interface structure leads to a transition of t_{2g} orbitals electrons, forming an electron-filled gap (e_g) orbital with an electron occupancy of one. This partially filled e_g orbital is conducive to enhancing the adsorption of sulphur intermediates on the FeCoNiMnMg–S surface, which fundamentally explains its high sulphur oxidation activity.

The catalytic performance is closely related to the adsorption energy of reaction intermediates.[50] For the SOR, adsorbed S^{2-} ions undergo gradual oxidation to form short-chain polysulfide intermediates, including S*, S_2*, S_3*, S_4*, and S_8* and are ultimately desorbed to produce S8 molecules. Based on the above analysis, Fig. S34 illustrates the stepwise oxidation mechanism of the SOR on the surface of FeCoNiMnMg–S nanosheet structures. The FeCoNiMnMg–S and NiS_2 catalyst models were optimized, and the Gibbs free energies of each step of the SOR (*i.e.*, * + S^{2-} → S* → S_2* → S_3* → S_4* → S_8*) were calculated. The specific adsorption configurations of the reaction intermediates are shown in Fig. S35 and S36. As illustrated in Fig. 4f, the adsorption of S^{2-} proceeds spontaneously, which may cause rapid accumulation of high concentrations of S* near the electrode surface. The conversions of S* to S_2* and S_4* to S_8* are endothermic and require overcoming substantial energy barriers. These steps constitute the rate-determining steps (RDSs) for FeCoNiMnMg–S and NiS_2, respectively. Compared with NiS_2 (1.93 eV), FeCoNiMnMg–S exhibits a lower energy barrier (1.69 eV) in the SOR, indicating higher SOR activity, consistent with the experimental electrocatalytic results. Furthermore, Bader charge analysis of S_8 molecules adsorbed on NiS_2 and FeCoNiMnMg–S reveals that the Ni atom in NiS_2 transfers 0.287*e*, considerably more than the 0.167*e* transferred in FeCoNiMnMg–S (Fig. 4g). This indicates that the doping of other elements weakened the interaction between the nickel sites and the S_8 molecules. This may be attributed to the

electron buffering effect of the accessible multivalent elements nearby, which alleviated the sulfur poisoning at the active nickel sites and thereby improved the SOR performance.

The HER performance of FeCoNiMnMg–S was also evaluated in a three-electrode cell using 1.0 M NaOH. As shown in Fig. S37a, FeCoNiMnMg–S exhibited an overpotential of 355 mV at a current density of 500 mA cm^{-2}, outperforming the other catalysts (FeCoNiMg–S: 375 mV, FeCoNi–S: 387 mV, Pt/C: 404 mV and NF: 473 mV). The Tafel slope shown in Fig. S37b indicates that the Tafel slope value of FeCoNiMnMg–S is significantly lower than that of the control sample, suggesting that the reaction kinetics of FeCoNiMnMg–S is faster. And further, using the LSV curves obtained for FeCoNiMnMg–S in 1.0 M NaOH solution as a reference, it can be observed that in the presence of 3.0 M Na_2S, current densities of 100 and 500 mA cm^{-2} are achieved at low potentials of 0.30 V and 0.42 V *vs.* RHE, respectively, which are 1.20 V and 1.15 V lower than those of the conventional OER (Fig. 5a). This indicates that the SOR has a thermodynamic advantage over the OER due to its lower oxidation potential and faster kinetics.

To achieve an energy-efficient dual-electrode hydrogen production system, a dual-electrode electrocatalytic coupling system was constructed by coupling the SOR with the HER, using FeCoNiMnMg–S as the anode and cathode catalysts, to replace the traditional OER (Fig. 5b and S38). As shown in Fig. 5c and d, when the OER is replaced by the SOR to pair with the HER, the required battery voltage can be significantly reduced from 1.61 and 1.87 V to 0.74 and 1.04 V, respectively, providing 100 and 1000 mA cm^{-2}. Compared with traditional alkaline water electrolysis, the HER + SOR system saves 0.87 V and 0.83 V of voltage, confirming its strong competitiveness in practical applications. In addition, stability tests conducted on the system at industrial-level current densities of 200 mA cm^{-2} for 200 hours of electrolysis showed no significant attenuation (Fig. 5e). FeCoNiMnMg–S||FeCoNiMnMg–S batteries exhibit superior activity and durability compared to recently reported coupled systems (Fig. 5f and Table S4). The cathode and anode materials after long-term electrolysis were characterized by SEM, and the morphology and elements showed no significant changes (Fig. S39). This further indicates that our catalytic system has good stability.

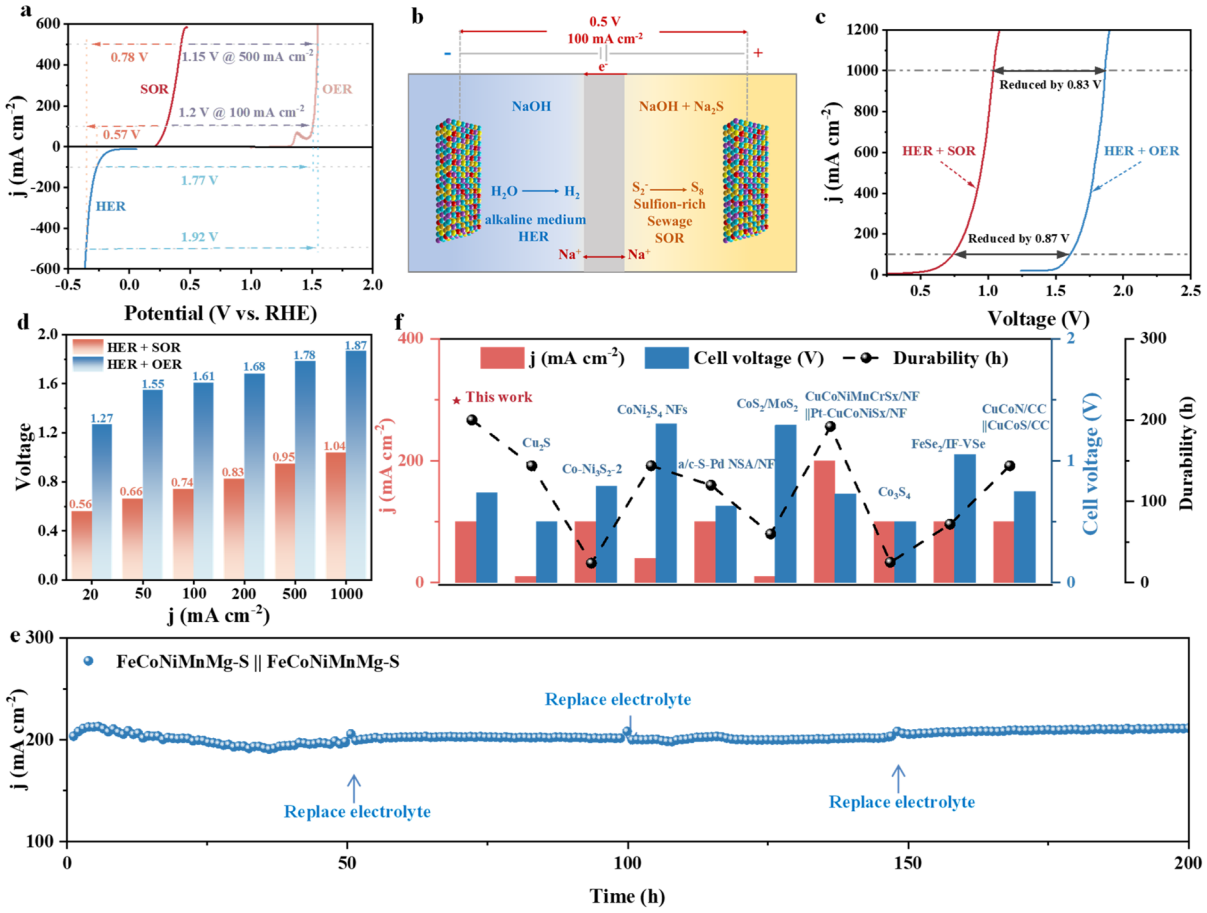

Fig. 5 (a) LSV curves of the HER, OER, and SOR tested using a three-electrode system, (b) schematic illustration of the electrolytic system using bifunctional FeCoNiMnMg–S electrodes in a 1.0 M NaOH with 3.0 M Na_2S solution (right) and H_2 evolution (left), (c) LSV curves of FeCoNiMnMg–S couple in 1.0 M NaOH with and without Na_2S in a two-electrode system, (d) histogram of cell voltages at 20, 50, 100, 200, 500 and 1000 mA cm^{-2}, (e) long-term stability testing of the HER + SOR system at a current density of 200 mA cm^{-2} (the anode and cathode electrolytes were replaced every 50 hours respectively), and (f) comparison of the cell voltage, current density, and durability with those of previously reported state-of-the-art electrocatalysts.

As the electrolysis time increased, the initial electrolyte gradually transformed from its original transparent and clear state to a deep yellow color. After 50 hours of electrolysis, the yellow anode powder was collected by acidifying the yellow electrolyte and was confirmed by XRD to be elemental sulfur (JCPDS no. 01-089-2600, Fig. S40a). The total yield was determined by weighing to be 1470 mg, with a yield of 117.6 mg h^{-1} cm^{-2}, and the average faradaic efficiency of the SOR was 98.5%. This also demonstrates the potential of FeCoNiMnMg–S catalytic hybrid electric systems to synergistically achieve hydrogen production at the cathode and sulfur production at the anode. To determine the mechanism of the SOR process, ultraviolet-visible (UV-vis) spectrophotometry was used to analyze the products in the electrolyte. As shown in Fig. S40b, distinct absorption peaks were observed at 300 and 370 nm, and the signal intensity of these peaks increased significantly with prolonged electrolysis time, confirming the presence of short-chain polysulfides (S_2*–S_4*) in the electrolyte.[14]

Conclusions

Amorphous/crystalline high-entropy heterostructured FeCoNiMnMg–S nanosheets were grown *in situ* on NF substrates *via* a one-step room-temperature vulcanization method. The obtained catalyst exhibits excellent electrocatalytic performance in the SOR. At a voltage of 0.30 V, the current density reaches 100 mA cm^{-2}, which is 1.21 V lower than that of the OER, and its stability exceeds 100 hours. When employed as both the cathode and anode in an alkaline water electrolyzer, the FeCoNiMnMg–S-based cell requires only 0.74 V to reach 100 mA cm^{-2}. This outstanding performance stems from the corrosion resistance and structural stability conferred by the high-entropy effect, coupled with a rapid charge transfer mechanism that triggers electronic rearrangement within the a–c heterostructure. Strong interfacial interactions enable enhanced redistribution of electrons within the 3d orbitals of metallic sites, thereby facilitating electron transfer at the a–c interface. Concurrently, this ensures rapid adsorption of reactants, transfer of intermediates, and swift release of products. This not only provides profound insights into the application mechanism of the a–c interface in the sulfur oxidation reaction, but also enables efficient and energy-saving hydrogen production as well as environmentally friendly sulfur ion recovery.

Author contributions

L. W. and H. L. conceived and supervised the project. R. L., J. L., Y. P., Y. L., and H. L. conducted the experiments. R. L., J. L., Y. P., Y. L., X. W., and D. Z. analysed the data and contributed to writing the manuscript.

Conflicts of interest

The authors declare no competing interests.

Data availability

The data that support the findings of this study are available on request from the corresponding author.

Supplementary information (SI): additional experimental and computational details, including morphology and elemental mapping, electrochemical performance, XPS, and theoretical calculation model. See DOI: https://doi.org/10.1039/d6sc02936a.

Acknowledgements

This work was supported by the National Natural Science Foundation of China (52472217, 52272222, and 22302108), Taishan Scholar Young Talent Program (tsqn202507195), and Youth Innovation and Technology Foundation of Shandong Higher Education Institutions, China (2023KJ313).

References

1 A. Odenweller and F. Ueckerdt, *Nat. Energy*, 2025, **10**, 110–123.
2 H. G. Han, J. W. Choi, M. Son and K. C. Kim, *eScience*, 2024, **4**, 100204.
3 J. Huang, B. Hu, J. Meng, T. Meng, W. Liu, Y. Guan, L. Jin and X. Zhang, *Energy Environ. Sci.*, 2024, **17**, 1007–1045.
4 J. Li, Y. Zhu, C. Li, Q. Zhang, J. Rong, S. Guo, N. Alonso-Vante, L. Yang, M.-H. Yeh, W.-H. Huang, X. Yu, H. Cheng and J. Ma, *Nat. Commun.*, 2025, **16**, 8827.
5 C. Rong, X. Huang, H. Arandiyan, Z. Shao, Y. Wang and Y. Chen, *Adv. Mater.*, 2025, **37**, 2416362.
6 Z. Hu, H. Wu, X. Yong, G. I. N. Waterhouse, Z. Tang, J. Chang, J. Chang and S. Lu, *eScience*, 2025, **5**, 100403.
7 G. Wang, X. Guo, L. Lyu, R. Gan, Y. Zheng, H. Lee and X. Shao, *Carbon Neutrality*, 2025, **4**, e70048.
8 L. Zhang, W.-Y. Wu, Q.-Y. Hu, S.-D. Yang, L. Li, R.-J. Liao and Z.-D. Wei, *J. Electrochem.*, 2025, **31**, 2515007.
9 B. Wu, W. Su, P. Zhu, J. Xu, K. Yuan, L. Li and Y. Chen, *Adv. Mater.*, 2025, **37**, e07842.
10 Q. Mai, Y. Mai, Y. Zhong, R. Xue, B. Jia, X. Guan, W. Du, H. Pan, Y. Li, Z. Zhang, L. Zhu, X. Li, P. Li and T. Ma, *Adv. Energy Mater.*, 2025, **15**, 2500415.
11 M. Li, H. Li, K. Xiang, J. Zou, X.-Z. Fu, J.-L. Luo, G. Luo and J. Zhang, *Electrochem. Energy Rev.*, 2025, **8**, 4.
12 J. Wang, X. Liu, C. Ma, X. Duan, S. Li, N. Li, W. Liu, Y. Li, X. Fan and W. Peng, *Adv. Funct. Mater.*, 2025, **35**, 2420157.
13 Y. Wang, K. Xu, Z. Zhu, W. Guo, T. Yu, M. He, W. Wei and T. Yang, *Chem. Commun.*, 2021, **57**, 1368–1371.
14 L. Zhang, Z. Wang and J. Qiu, *Adv. Mater.*, 2022, **34**, 109321.
15 H. Liu, X. Liu, A. Sun, C. Xuan, Y. Ma, Z. Zhang, H. Li, Z. Wu, T. Ma and J. Wang, *Adv. Mater.*, 2025, **37**, 2501186.
16 N. Kar and S. E. Skrabalak, *Nat. Rev. Mater.*, 2025, **10**, 638–653.
17 G. Wang, Z. Chen, J. Zhu, J. Xie, W. Wei, Y.-M. Yan and B.-J. Ni, *Nano-Micro Lett.*, 2025, **18**, 77.
18 Q. Xie, Y.-J. Yu, H.-J. Zhang, Y.-P. Deng and W. Lei, *Tungsten*, 2024, **7**, 1–31.

19 D. Zhang, Y. Shi, X. Chen, J. Lai, B. Huang and L. Wang, *Chin. J. Catal.*, 2023, **45**, 174–183.
20 H. Cai, S. He, H. Yang, Q. Huang, F. Luo, Q. Hu, X. Zhang and C. He, *Adv. Mater.*, 2025, **37**, 2508610.
21 Y. Pei, D. Li, C. Qiu, L. Yan, Z. Li, Z. Yu, W. Fang, Y. Lu and B. Zhang, *Angew. Chem., Int. Ed.*, 2024, **63**, e202411977.
22 Y. Liu, J. Liu, E. Zhou, D. Liu, J. Cui, B. Li, Y. Du, L. Yang, G. Liang, H. Lv and R. Che, *Adv. Funct. Mater.*, 2025, **36**, e14873.
23 Z. Yang, B. Wang, Y. Chen, W. Zhou, H. Li, R. Zhao, X. Li, T. Zhang, F. Bu, Z. Zhao, W. Li, D. Chao and D. Zhao, *Natl. Sci. Rev.*, 2022, **10**, nwac268.
24 W. Peng, S. Li, Y. Li, C. B. Musgrave Iii, B. Yuan, B. A. Shah, R. Hu, W. A. Goddard Iii, Z. Luo and M. Zhu, *Appl. Catal., B*, 2025, **363**, 124777.
25 Y. Shen, Y. C. Huang, Y. Wang, H. He, Z. Yu, Z. Jia, M. Ma, H. Zhou, P. Du, Y. Liu, C. L. Dong and S. Shen, *Adv. Energy Mater.*, 2026, **16**, e04886.
26 M. Liu, H. Su, X. Liu, X. He, P. Tan, F. Liu and J. Pan, *Nat. Commun.*, 2025, **16**, 2826.
27 P. Tian, W. Zong, J. Xiong, W. Liu, J. Liu, Y. Dai, J. Zhu, S. Huang, S. Song, K. Chu, G. He and N. Han, *Adv. Funct. Mater.*, 2025, **35**, 2504862.
28 X. Chen, Y. Du, Y. Yang, K. Liu, J. Zhao, X. Xia and L. Wang, *Chin. J. Catal.*, 2024, **62**, 265–276.
29 H. Li, R. Meng, C. Ye, A. Tadich, W. Hua, Q. Gu, B. Johannessen, X. Chen, K. Davey and S. Z. Qiao, *Nat. Nanotechnol.*, 2024, **19**, 792–799.
30 J. P. Singh, J. Y. Park, K. H. Chae, D. Ahn and S. Lee, *Nanomaterials*, 2020, **10**, 759.
31 P. Gu, Y. Song, Y. Fan, X. Meng, J. Liu, G. Wang, Z. Li, H. Sun, Z. Zhao and J. Zou, *Adv. Energy Mater.*, 2025, **15**, 2403657.
32 Y. Gao, X. Sun, G. A. M. Mersal, A. Alhadhrami, M. M. Ibrahim, Y. Hou, W. Liu, D. Bildan, H. Algadi and T. X. Liu, *Adv. Compos. Hybrid Mater.*, 2025, **8**, 117.
33 W. Peng, Y. Li, B. Yuan, R. Hu, Z. Luo and M. Zhu, *Appl. Catal., B*, 2023, **323**, 122171.
34 C. Li, N. Wang, S. Wang, C. Li, W. Fan, T. Liu, S. Chen and F. Zhang, *Adv. Funct. Mater.*, 2025, **35**, 2423856.
35 J. Wang, M. Zhou, R. Fu, J. Ge, W. Yang, X. Hong, C. Sun, X. Liao, Y. Zhao and Z. Wang, *Adv. Funct. Mater.*, 2024, **34**, 2315326.
36 F. Nur Indah Sari, M.-T. Ke, Y.-J. Huang, T.-M. Zheng, Y.-H. Su and J.-M. Ting, *Appl. Surf. Sci.*, 2024, **649**, 159187.
37 F. N. Indah Sari, S. Marsaor Sihotang, S.-Y. Li, Y.-H. Shen and J.-M. Ting, *ACS Sustainable Chem. Eng.*, 2023, **11**, 1207–1220.
38 M. Cui, C. Yang, B. Li, Q. Dong, M. Wu, S. Hwang, H. Xie, X. Wang, G. Wang and L. Hu, *Adv. Energy Mater.*, 2020, **11**, 2002887.
39 C. Feng, M. Chen, Y. Zhou, Z. Xie, X. Li, P. Xiaokaiti, Y. Kansha, A. Abudula and G. Guan, *J. Colloid Interface Sci.*, 2023, **645**, 724–734.
40 K. Fan, H. Zou, Y. Lu, H. Chen, F. Li, J. Liu, L. Sun, L. Tong, M. F. Toney, M. Sui and J. Yu, *ACS Nano*, 2018, **12**, 12369–12379.
41 X. Bai, M. Zhang, Y. Shen, X. Liang, W. Jiao, R. He, Y. Zou, H. Chen and X. Zou, *Adv. Funct. Mater.*, 2024, **34**, 2400979.
42 W. H. Yun, G. Das, B. Kim, B. J. Park, H. H. Yoon and Y. S. Yoon, *Sci. Rep.*, 2021, **11**, 22003.
43 F. N. I. Sari, Y. C. Lai, Y. J. Huang, X. Y. Wei, H. Pourzolfaghar, Y. H. Chang, M. Ghufron, Y. Y. Li, Y. H. Su, O. Clemens and J. M. Ting, *Adv. Funct. Mater.*, 2024, **34**, 2310181.
44 L. Lin, Z. Ding, G. Karkera, T. Diemant, M. V. Kante, D. Agrawal, H. Hahn, J. Aghassi-Hagmann, M. Fichtner, B. Breitung and S. Schweidler, *Small Struct.*, 2023, **4**, 2300012.
45 T. X. Nguyen, Y. H. Su, C. C. Lin and J. M. Ting, *Adv. Funct. Mater.*, 2021, **31**, 2106229.
46 M. Song, X. Yang, C. Guo, S. Zhang, J. Ma and H. Gao, *EcoEnergy*, 2025, **3**, 470–481.
47 W. Liu, W. Tan, H. He and Y. Yang, *Electrochim. Acta*, 2022, **411**, 140058.
48 E. Sadeghi, N. S. Peighambardoust, M. Khatamian, U. Unal and U. Aydemir, *Sci. Rep.*, 2021, **11**, 3337.
49 X. Tian, R. Liu, W. Wang, Q. Yang, Z. Huang, Y. Yang, J. Han, T. Dong, Y. Du, J. Lai, H. Li and L. Wang, *Adv. Mater.*, 2025, **37**, e06068.
50 R. Chang, Y. Pang, Q. Yang, R. Liu, Y. Yang, Y. Du, K. Liu, Z. Wu, J. Lai, H. Li and L. Wang, *Chem. Sci.*, 2025, **16**, 11961–11969.
51 Y. Pei, J. Cheng, H. Zhong, Z. Pi, Y. Zhao and F. Jin, *Green Chem.*, 2021, **23**, 6975–6983.
52 K. Yang, N. Zhang, J. Yang, Z. Xu, J. Yan, D. Li and S. Liu, *Appl. Catal., B*, 2023, **332**, 122718.
53 L. Fang, Y. Zhang, Y. Guan, H. Zhang, S. Wang and Y. Wang, *J. Mater. Chem. A*, 2017, **5**, 2861–2869.
54 X. Zhou, H. Zhu, S. Fu, S. Lan, H. Hahn, J. Zeng and T. Feng, *Small*, 2024, **20**, 2405596.
55 S. Yang, X. Liu, S. Li, W. Yuan, L. Yang, T. Wang, H. Zheng, R. Cao and W. Zhang, *Chem. Soc. Rev.*, 2024, **53**, 5593–5625.
56 M. Ismail, S. Manseri, M. Jin, B. Guo, H. Liu, Y. Zhu, X. Ma, C. Cao and M. Zou, *J. Power Sources*, 2025, **651**, 237506.
57 J. Kwon, S. Sun, S. Choi, K. Lee, S. Jo, K. Park, Y. K. Kim, H. B. Park, H. Y. Park, J. H. Jang, H. Han, U. Paik and T. Song, *Adv. Mater.*, 2023, **35**, 2300091.
58 D. Merki, S. Fierro, H. Vrubel and X. Hu, *Chem. Sci.*, 2011, **2**, 1262–1267.
59 R. Liu, Q. Yang, Y. Pang, H. Li, Y. Liu, W. Wang, Z. Wang, R. Chang, X. Tian, J. Lai and L. Wang, *Small*, 2025, **21**, 2500518.
60 T. Jiang, M. Qu, X. Liu, W. Du, S. Cha, Y. Meng, X. Zhou, Z. Deng and M. Gong, *Nat. Synth.*, 2026, DOI: 10.1038/s44160-026-01047-y.
61 S. Lyu, W. Wu, R. Xiong, C. Yang, B. Sa, J. Zhang, Y. Hou and X. Wang, *J. Catal.*, 2022, **413**, 992–1004.
62 T. Cui, X. Zhai, L. Guo, J.-Q. Chi, Y. Zhang, J. Zhu, X. Sun and L. Wang, *Chin. J. Catal.*, 2022, **43**, 2202–2211.
63 J. Hu, T. Guo, X. Zhong, J. Li, Y. Mei, C. Zhang, Y. Feng, M. Sun, L. Meng, Z. Wang, B. Huang, L. Zhang and Z. Wang, *Adv. Mater.*, 2024, **36**, e2310918.
64 M. W. Gu, C. T. Lai, I. C. Ni, C. I. Wu and C. H. Chen, *Angew. Chem., Int. Ed.*, 2023, **62**, e202214963.